



# Determination of physically based pseudo-Voigt powder diffraction profile terms from the fundamental parameters approach

Jonathan J. Denney, Gerard S. Mattei, Marcus H. Mendenhall, James P. Cline, Peter G. Khalifah and Brian H. Toby

*J. Appl. Cryst.* (2022). **55**, 289–295

# Determination of physically based pseudo-Voigt powder diffraction profile terms from the fundamental parameters approach

Jonathan J. Denney,<sup>a,b</sup> Gerard S. Mattei,<sup>a,b</sup> Marcus H. Mendenhall,<sup>c</sup> James P. Cline,<sup>c</sup> Peter G. Khalifah<sup>a,b</sup> and Brian H. Toby<sup>d\*</sup>

Received 4 August 2021  
Accepted 1 February 2022

<sup>a</sup>Stony Brook University, 100 Nicolls Road, Stony Brook, NY 11794, USA, <sup>b</sup>Brookhaven National Laboratory, Upton, NY 11793, USA, <sup>c</sup>National Institute of Standards and Technology, 100 Bureau Drive Stop 8523, Gaithersburg, MA 20899, USA, and <sup>d</sup>Argonne National Laboratory, 9700 South Cass Avenue, 401/B4192, Lemont, IL 60439, USA.

\*Correspondence e-mail: brian.toby@anl.gov

Edited by T. J. Sato, Tohoku University, Japan

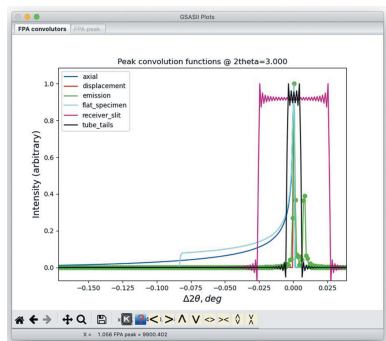
**Keywords:** powder diffraction; fundamental parameters; Rietveld analysis; *GSAS-II*.

A methodology is developed where a fundamental parameters approach (FPA) description of a laboratory powder diffraction instrument (configured in divergent-beam Bragg–Brentano geometry) is used to determine *GSAS-II* profile parameters for peak asymmetry and instrumental peak widths. This allows the instrumental contribution to peak shapes to be robustly determined directly from a physical description of the instrument, even though *GSAS-II* does not directly implement FPA for peak shape computation. The FPA-derived parameters can be used as the starting point for instrument characterization, or to characterize sample broadening without the use of a standard to determine the instrument profile function. This new method can facilitate generation of training sets for machine learning. A plot is generated that shows the differences between the two approaches, demonstrating upper bounds for the accuracy of the *GSAS-II* profile model for a particular instrumental configuration.

## 1. Introduction

There have been a number of approaches employed for describing peak profile shapes in powder diffraction. Initial work was generally physics based but sometimes also used empirical approximations for poorly understood or difficult to model behaviour. Cagliotti *et al.* (1958) found that, for constant-wavelength (CW) neutrons and ideally mosaic monochromators, the instrumental resolution can be expected to produce Gaussian diffraction peaks, where the widths change according to what was later expressed as a power law in  $\tan\theta$  (Rietveld, 1967) or, better still, a power law in  $\tan(\theta - \theta_m)$ , where  $\theta_m$  is the monochromator take-off setting (Prince, 2004). Instrument profile models were further improved through the introduction of an *ad hoc* correction for low-angle peak asymmetry (Rietveld, 1967). That asymmetry correction was later replaced with an improved physics-based model for axial divergence (van Laar & Yelon, 1984; Eddy *et al.*, 1986; Finger *et al.*, 1994). In practice, both X-ray and neutron instrumental peak shapes may have both Gaussian and Cauchy (Lorentzian) components.

In addition to being influenced by the instrument configuration, observed powder diffraction peak shapes are determined by sample broadening, predominantly from two sources: Scherrer broadening, due to finite crystallite sizes (Scherrer, 1918; Patterson, 1939), and microstrain, where non-equilibrium conditions cause some domains to be under tension while others have residual stress (Kochendörfer, 1943;



Klug & Alexander, 1974). Broadening can arise from sample properties such as composition gradients or local ordering. Note that both size and microstrain broadening can be anisotropic, meaning that they have differing magnitudes depending on the reciprocal-space direction of individual reflections. Size and microstrain broadening are most commonly Cauchy in nature but may have a more complex shape depending on column-length distributions (Bertaut, 1950; Kril & Birringer, 1998; Scardi & Leoni, 2001). Analytical functions may not fully describe peak shapes in the presence of very complex ordering phenomena such as stacking faults.

When it came to fitting peak profiles, the field initially split between practitioners who selected completely *ad hoc* peak shapes with no physics behind them, such as a split Pearson VII function or functions ‘learned’ to match data (Baerlocher, 1982), and others who used physically derived (PD) approximant functions such as the computationally expensive Voigt function, which is a convolution of a Lorentzian and a Gaussian (Langford, 1978). Later it was shown that the ‘pseudo-Voigt’ function, which is a sum of Gaussian and Lorentzian functions and is a good approximation to the Voigt, could be parameterized in terms of Voigt components (Hastings *et al.*, 1984; David, 1986). Most contemporary powder diffraction peak fitting programs, including the majority of Rietveld refinement packages, now implement PD approximant peak shape descriptions (Rietveld, 1969; Hewat, 1973; Finger & Prince, 1975; Wiles & Young, 1981; Rodríguez-Carvajal, 1993; Izumi & Ikeda, 2000; Larson & Von Dreele, 2004; Petříček *et al.*, 2006; Coelho, 2007; Tian *et al.*, 2013; van Laar & Schenk, 2018). The peak shapes are described using PD parameters, where the widths are formulated as a series of polynomial terms in functions of  $2\theta$  for CW X-ray and neutron instruments, or functions of time of flight (TOF) for TOF neutron instruments. Some of these polynomial terms combine broadening contributions from both the instrument and the sample (Larson & Von Dreele, 2004; Kaduk & Reid, 2011).

A more recent development, implemented in the open-source *GSAS-II* program (Toby & Von Dreele, 2013), separates sample and instrumental contributions into separate equations. While *GSAS-II* can be used in the same fashion as older Rietveld programs where most or all profile terms are refined, the preferred mode for use of *GSAS-II* is to determine the instrumental profile function (IPF), usually by fitting profile parameters to data from a standard with known sample broadening contributions (*e.g.* Black *et al.*, 2011). Once the IPF has been appropriately characterized, only the sample broadening contributions need be determined. This both simplifies the fitting process and allows direct interpretation of sample broadening. It also allows for quite sophisticated characterization of Scherrer and microstrain broadening, where each offers choices between an isotropic and two anisotropic broadening models. The preferred workflow for *GSAS-II* is that the IPF coefficients are determined for a specific instrumental configuration and saved as an instrument parameter file, which is used subsequently when reading diffraction data that have been collected using that instrumental configuration. To determine the IPF coefficients, one

collects a diffraction pattern from a sample known to have minimal sample broadening, such as the NIST 660 series Standard Reference Materials (Black *et al.*, 2011), and the profile terms are fitted to these data. Since the profile terms tend to have high correlations, they can be somewhat difficult to refine, so it can sometimes be useful to start with a fit to individual peaks. An online tutorial for *GSAS-II* is provided that illustrates this process (<https://subversion.xray.aps.anl.gov/pyGSAS/Tutorials/CWInstDemo/FindProfParamCW.htm>). This approach can also be helpful when fitting profile terms directly to data for a sample without fitting the IPF. The instrumental coefficients, once determined, may then be considered as fixed constants. This greatly simplifies the process of profile fitting in Rietveld analysis, as only sample broadening terms need be refined. However, any change to the instrumental configuration, such as adjusting the width of the divergence slit, will change the IPF, requiring that new calibration data be collected from a diffraction standard to redetermine the IPF coefficients.

An alternative approach for fitting peak profiles, called the fundamental parameters approach (FPA), originated with the work of Wilson (1963). Cheary and others made this approach accessible through software packages (Cheary & Coelho, 1992; Bergmann *et al.*, 1998; Petříček *et al.*, 2006; Coelho, 2007). In FPA, each source of peak broadening in the X-ray diffraction experiment, such as those arising from the incident X-ray spectrum, the slits and collimation, focusing and parafocusing contributions, detector effects, and sample size and microstrain contributions, has its aberration contribution defined quantitatively on the basis of a physical description of the X-ray optical component. While historically these effects have been used qualitatively to understand observed peak shapes (Klug & Alexander, 1974), in FPA each of these contributions is parameterized on the basis of physical models, and only the undetermined factors (such as sample broadening) need be optimized to fit diffraction patterns. FPA is widely used for traditional laboratory powder diffraction instruments with a point or strip detector, where all the scattering occurs in a single plane, particularly as implemented in the *TOPAS*<sup>1</sup> Rietveld program (Coelho, 2007, 2018). For TOF and synchrotron instruments, which may have a larger number of optical components, PD parameters are commonly used in place of FPA descriptions. In addition to the commercial *TOPAS* software, the FPA approach is also implemented in the freely available *JANA* Rietveld package (Petříček *et al.*, 2006). Alternatively, the profiles of individual peaks can be computed from an FPA instrument description using the rigorously validated and fully open source NIST FPA code (Mendenhall *et al.*, 2015).

The FPA approach provides a more general approach to peak shapes, so that FPA models are able to fit highly complex peak shapes resulting from subtle instrumental contributions

<sup>1</sup> Certain commercial instruments, materials or processes are identified to adequately specify the experimental procedure. Such identification does not imply recommendation or endorsement by the National Institute of Standards and Technology, nor does it imply that the instruments, materials or processes identified are necessarily the best available for the purpose.

Table 1

Fundamental parameter definitions for Bragg–Brentano diffraction following *TOPAS* usage, as employed for input for the *GSAS-II* FPA implementation, along with usage suggestions.

Note that the axial direction is parallel to the rotation axis that specifies  $\theta$  and  $2\theta$  in the diffractometer, and the equatorial plane is perpendicular to that axis. The radial direction is the normal to the sample plane, e.g. the direction from the sample to the X-ray source at  $2\theta = 0$ .

Parameter name	Units	Description
Bragg–Brentano – parameters for instrument and slits/collimators		
Rs	mm	Diffractometer radius; assumes equal source-to-sample and sample-to-detector distances
Divergence	°	Divergence in axial plane (determined by a fixed-width slit) for the X-ray source
soller_angle	°	Maximum divergence in equatorial plane permitted by Soller slits (collimators)
Bragg–Brentano – parameters for source (and its interactions with sample)		
filament_length	mm	Length of X-ray filament along its long axis for tube used in ‘line-focus’ direction
sample_length	mm	Length of sample illuminated by X-ray beam in axial direction; if slits do not limit this, it will match the filament length
receiving_slit_length	mm	Length of receiving slit in axial direction; if receiving slit does not limit this, it will match the sample length
source_width	mm	Width of X-ray filament in projection in the equatorial plane
tube-tails_L-tail	mm	Width for X-ray intensity occurring beyond the Wehnelt shadow as a projection in the axial direction and measured in the positive $2\theta$ direction
tube-tails_R-tail	mm	Width for X-ray intensity occurring beyond the Wehnelt shadow as a projection in the axial direction and measured in the negative $2\theta$ direction
tube-tails_rel-I	(none)	Fraction of X-ray intensity found in the tube tails versus the main peak; note that tube tails are modelled as a step function
Bragg–Brentano – sample transparency correction		
LAC_cm	cm <sup>-1</sup>	Linear absorption coefficient of the sample, including possible correction for packing density (typically 30–60% of the theoretical density); a useful calculation tool is available at <a href="https://11bm.xray.aps.anl.gov/absorb/absorb.php">https://11bm.xray.aps.anl.gov/absorb/absorb.php</a>
sample_thickness	mm	Thickness of sample measured perpendicular to the equatorial plane; typical smear samples are 0.05–0.30 mm thick
Point detector parameter – when selected		
receiving_slit_width	mm	Height of receiving slit (perpendicular to axial direction) that controls acceptance to the detector (or alternatively, acceptance to a diffracted beam monochromator)
Linear position-sensitive detector (PSD) parameters – when selected		
lpsd_th2_angular_range	°	Angular ( $2\theta$ ) range in the equatorial plane subtended by the entire active region of the PSD
lpsd_equatorial_divergence	°	Divergence of the X-ray beam in the equatorial plane
SiPSD_th2_angular_range	°	Angular ( $2\theta$ ) range in the equatorial plane that the entire PSD subtends (not implemented in <i>TOPAS</i> )
Incident-beam monochromator (IBM) parameters – when selected		
src_mono_mm	mm	Distance between the X-ray source (filament) and the monochromator, measured in the equatorial plane
focus_mono_mm	mm	Distance from monochromator crystal to focus slit, measured in the equatorial plane
passband_mistune	(none)	Offset for the tuning of the IBM to the centre of the reference line of the spectrum, as a fraction of the IBM bandwidth
mono_src_proj_mm	µm	Bandwidth setting for the monochromator as set by the projection width of the X-ray source on the monochromator along the beam direction and in the equatorial plane
passband_shoulder	(none)	Width of the transition region from the high-intensity roughly flat region of the X-ray tube output to the tube tail region, as a fraction of the IBM bandwidth
two_theta_mono	°	The full diffraction angle of the IBM crystal; this will be double the Bragg $2\theta$ angle for the monochromator
mono_slit_attenuation	(none)	The attenuation of the Cu $K\alpha_2$ source lines relative to the $K\alpha_1$ lines, as determined by the focal slit
Calculation precision setting		
convolution_steps	(none)	The number of steps used for convolution for each step (i.e. in $2\theta$ ) in the diffraction pattern; this results in smoother convolutions

that cannot be fitted well within the PD approach. The FPA method has proven irreplaceable for high-accuracy characterization of diffraction instrumentation, where diffraction performance must be related to the performance of the instrument optics (Black *et al.*, 2011; Cline *et al.*, 2019). However, the difference between these approaches is less significant when the goal of the experiment is to investigate a crystal structure through Rietveld refinement. In practice and by design, commercial diffraction instruments generally have regular peak shapes that can be fitted well with only small errors using PD approaches, even if FPA does provide a slightly better match to observed peak shapes. The slightly lower quality fit that is obtained from the PD peak shape causes only very small intensity mismatches. Further, these effects tend to be quite consistent across all peaks. Thus, the

optimized structural models obtained from PD versus FPA fitting are typically indistinguishable.

In this work we describe a new approach for peak profile generation, combining the physically based and fundamental parameter methods, using the aforementioned open-source *GSAS-II* and NIST FPA codes. Here we use FPA to generate the *GSAS-II* peak shape parameters, which allows many of the benefits of FPA when carrying out refinements utilizing the capabilities provided by the widely used and freely available *GSAS-II* refinement engine. This implementation is specific for constant-wavelength diffraction and has been demonstrated here for Bragg–Brentano instruments, but other types of instrument could also be utilized, provided that the NIST FPA code offers the appropriate convolvers needed to model their optical descriptions.

## 2. Method

Our new approach allows direct computation of the *GSAS-II* profile parameters that describe the IPF from FPA parameters for an instrument. A graphical user interface (GUI) in *GSAS-II* permits the input of FPA descriptors in units fashioned to follow the conventions of *TOPAS*. These parameters are tabulated in Table 1. The parameter values are then reformulated into SI units so they can be utilized in the NIST FPA code, as shown in Fig. 1. The NIST FPA code can then be used to generate peak profiles, with the results read into *GSAS-II* as a powder diffraction histogram (data set). An automated peak fitting process is then invoked, wherein the reflection positions and intensities are fitted individually for each profile and a global set of profile parameters (*U*, *V*, *W* for Gaussian peak widths, *X* and *Y* for Cauchy widths and the *SH/L* parameter

```
# parameters to be used in the NIST XRD Fundamental
# Parameters program
{
  '' : {
    'diffractometer_radius': 0.22,
    'equatorial_divergence_deg': 0.5,
    'oversampling': 8, 'dominant_wavelength':
      1.540596e-10
  }, # global parameters
  'axial' : { 'angI_deg': 2.0, 'axDiv': 'full',
    'angD_deg': 2.0, 'n_integral_points': 10,
    'slit_length_target': 0.012000120000000001,
    'length_sample': 0.012,
    'slit_length_source': 0.012},
  'emission' : {
    'emiss_lor_widths': array([3.6854e-13,
      4.3700e-14, 6.0000e-14, 5.2000e-14, 6.2000e-14]),
    'emiss_intensities': array([0.0274564 , 1.,
      0.13158349, 0.41737178, 0.1504058 ]),
    'crystallite_size_lor': 0.001,
    'emiss_wavelengths': array([1.534753e-10,
      1.540596e-10, 1.541058e-10, 1.544410e-10,
      1.544721e-10]),
    'emiss_gauss_widths': array([1.e-16, 1.e-16, 1.e-16,
      1.e-16, 1.e-16]),
    'crystallite_size_gauss': 0.001},
  'receiver_slit' : { 'slit_width': 0.0002},
  'si_psd' : {
    'si_psd_window_bounds': (0.0,0.011524442978417064),
    'equatorial_divergence_deg': 0.1},
  'tube_tails' : {
    'tail_intens': 0.001, 'tail_left': 0.001,
    'main_width': 4e-05, 'tail_right': 0.001},
}
```

**Figure 1**  
Fundamental parameters as used as input to the NIST FP code. This is taken from a copy of the file used for input and output of parameters. Indentation and line breaks have been added to allow more simple visual interpretation.

for peak asymmetry) are determined. These resulting profile parameters constitute a best fit to the IPF in the *GSAS* (Larson & Von Dreele, 2004) and *GSAS-II* description. These parameters may then be used for the direct determination of the sample-dependent size and strain parameters without the need for a peak shape standard. Note that surface roughness is not implemented in the NIST code. This is because the surface roughness of a sample is rarely, if ever, measured directly and primarily affects the intensities of very low angle peaks. Surface roughness has only a very minor effect on peak profiles and again only at low diffraction angles. Roughness contributions to diffraction intensities can be corrected for in *GSAS-II*.

This new capability is accessed in *GSAS-II* under the 'Import' → 'Powder Data' menu, where there is an entry 'Fit instrumental profile from fundamental parameters.' This brings up a GUI window, as shown in Fig. 2, where the values needed for pattern generation are entered: the starting, ending and step  $2\theta$  values, the number of peaks to be generated, and the width to compute each peak. This window also offers two options for supplying FP input. Most commonly a dialogue window will be opened, as shown in Fig. 3, where *TOPAS*-style FP values are entered. This window also offers an option for plotting of the individual aberration functions used for convolution, as shown in Fig. 4, as well as the resulting peak at a particular  $2\theta$  location. The FPA input values are recast as a Python dict with SI units (see Fig. 1). This dict is directly transferred as input to the NIST FPA code. As an option, the FP input can be saved as an ASCII file for reuse. This file could be manually edited, which could allow access to future NIST FPA input options that may not be included in the GUI. Alternatively, this FPA input can be automatically generated

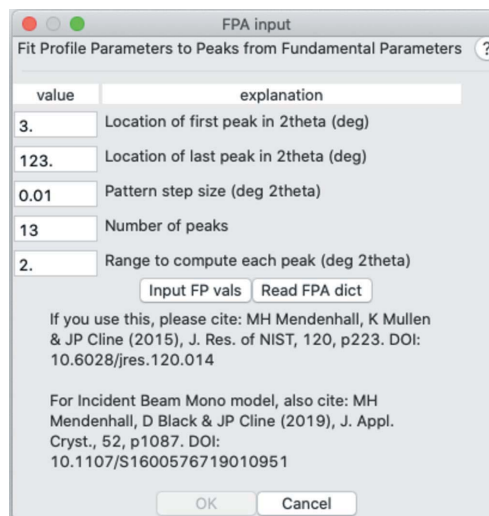


**Figure 2**  
The GUI for pattern generation input in *GSAS-II*. The input FPA parameters can be read from a previously saved set of values using the 'Read FPA dict' button or edited using the 'Input FP vals' button, which creates the window shown in Fig. 3. Once the FPA input is set and the 'OK' button is pressed, the peaks are generated and fitted with no further input. The button labelled with a question mark opens a web browser with documentation on this feature.

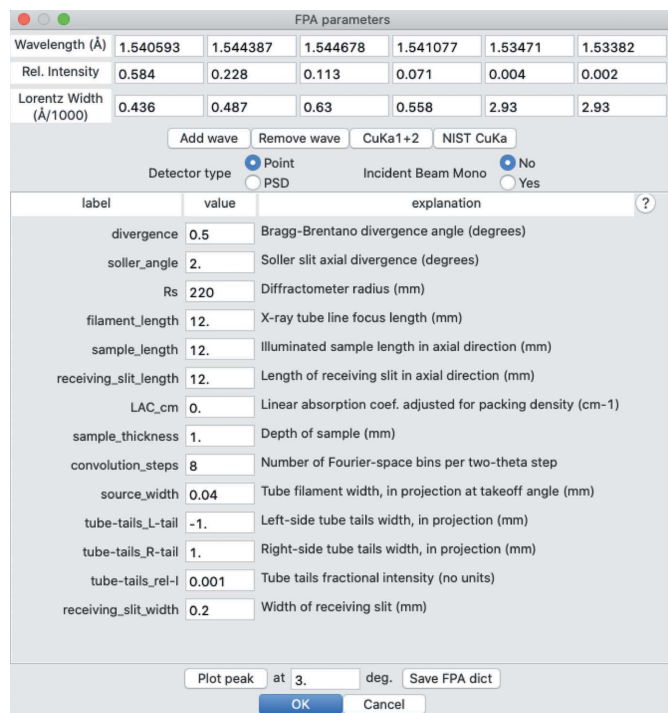


Figure 3

The GUI for TOPAS-style FPA input in GSAS-II. The 'Save FPA dict' button allows the input values to be saved to a file for later reuse. The 'Plot peak' button generates the graphical output shown in Fig. 4. The button labelled with a question mark provides documentation on the parameters listed in Table 1. The OK button closes this input window, returning to the window shown in Fig. 2. Note that the displayed parameters will depend on the selected options for the detector and monochromator.

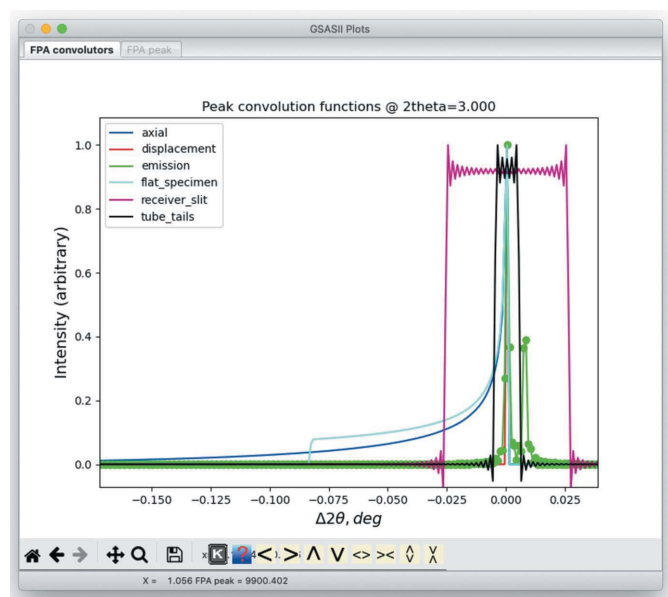


Figure 4

A plot of individual aberration functions generated from input supplied in Fig. 3. Note that, to help distinguish the individual items in this plot, clicking on an item in the legend highlights the corresponding item in the plot by plotting points, as shown here for the incident X-ray spectrum convolver.

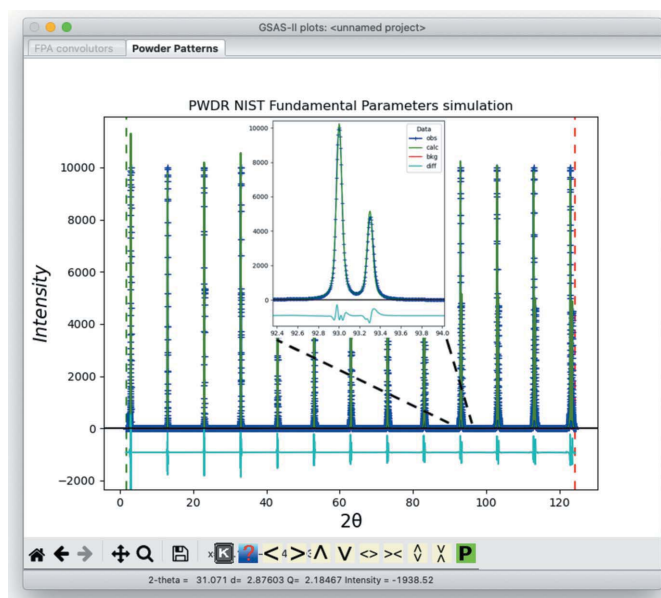


Figure 5

The plot generated by GSAS-II showing the pattern constructed from FPA computed peaks (blue crosses), the pattern fit using PD peak profiles (green line) and the differences between the two (cyan line at bottom). This capability demonstrates the discrepancies between the FPA-generated profile and what the GSAS-II profile model is able to generate. The inset shows one peak magnified, as is displayed by 'zooming in.'

by applications (such as training machine learning models) that require the generation of a multitude of diffraction data sets.

After the FPA input has been supplied, the powder pattern step size is checked to make sure that there are a sufficient number of points across each peak. If not, the step size is automatically decreased. Once the input has been accepted, the desired pattern is generated and the peaks are fitted automatically. The agreement between the FPA-generated pattern and the pattern fitted to it is plotted in a manner analogous to Rietveld refinement, as shown in Fig. 5, demonstrating the quality of the pseudo-Voigt PD fit to the FPA-generated pattern. Finally, the program requests a file name to be used to save the generated GSAS-II IPF values as an instrument parameter file; this file may be used as a starting point for fits to other diffraction patterns acquired using the modelled diffractometer configuration. Further fitting of the pattern is possible manually within the 'Peak List' section of GSAS-II, but this is unlikely to be needed. The GSAS-II FPA capability is also included in the GSAS-II scripting applications interface, which is documented separately (<https://gsas-ii.readthedocs.io/en/latest/GSASIIGUI.html#gsasiifpagui-fundamental-parameters-routines>). This allows this capability to be automated or incorporated into other codes.

### 3. Discussion and conclusions

This work has shown how the fundamental parameter and physically derived parameter approaches to powder diffraction peak shapes may be used together. The FPA may now be

utilized within *GSAS-II* to derive the expected instrument profile functions. There are two ways that this can be used: (i) with a very accurate instrumental description, the derived instrumental parameters will allow direct and accurate estimation of crystallite size and microstrain in samples, or (ii) with a fairly generic instrumental description, this will provide a good place to start the refinement of instrumental terms when initially fitting data from a standard or where data must be fitted without standardizing the instrument. Case (i) allows for direct adjustment of the IPF for sample transparency, taking into account the sample's as-packed linear absorption coefficient; calibration of the IPF with a standard will provide optimal agreement only when the standard's absorption matches that of the sample. Case (ii) has particular value to novice users of Rietveld refinement, who may find the IPF calibration to be a daunting (if not a terminal) barrier to carrying out structural analyses, given both the lack of a clear relationship between the physical geometry of an X-ray diffractometer and these terms and the high degree of correlation between them, which can lead to refinement instability or false minima. Another potential use for this capability will be to determine how well peak profiles from a particular instrument design can be fitted with a traditional PD pseudo-Voigt peak shape description. Further, the possibility of simulating diffraction patterns based on a set of FPA-derived parameters, directly derived for a given instrumental configuration, along with user-specified crystallite size and microstrain broadening input, opens new opportunities for the automated generation of the large quantities of labelled training data that are required for machine learning approaches to pattern analysis, such as automated indexing or structure solution from powder diffraction data (Mattei *et al.*, 2020; Szymanski *et al.*, 2021). Since this allows profile terms to be generated, this enables complete simulation of all aspects of the diffraction experiment. The ability of *GSAS-II* to run on a variety of platforms (with native versions for Intel-compatible Windows, Intel- and Arm-based Mac, Intel-compatible Linux and Raspberry Pi), as well as its capability to be run from scripts as an alternative to the GUI, makes it particularly suitable for these efforts, which often require batch access to computational clusters.

While current users of *GSAS-II* are best poised to utilize this new capability, some other programs use closely related formulations for the profile equations, and formulae for some common conversions have been tabulated (Kaduk & Reid, 2011). This allows peak profile terms determined in *GSAS-II* with this hybrid FPA/PD process to be used in other Rietveld programs. Finally, all the code discussed here is distributed as open source, so the work presented here can serve as a starting point for transfer of this capability into other packages.

#### 4. Distribution

The code described here, including a Python module with the NIST FPA implementation, is included in *GSAS-II*, which is distributed as open source with no fees charged for any type of academic or commercial use. It can be downloaded and

installed via instructions found at <https://subversion.xray.aps.anl.gov/trac/pyGSAS>. A tutorial demonstrating use of this new capability is also provided (<https://subversion.xray.aps.anl.gov/pyGSAS/Tutorials/FPAfit/FPAfit.htm>).

#### Acknowledgements

BHT would like to acknowledge his long-term collaboration with Robert B. Von Dreele that has allowed *GSAS-II* to be created.

#### Funding information

Use of the Advanced Photon Source, an Office of Science User Facility operated for the US Department of Energy (DOE) Office of Science by Argonne National Laboratory, was supported by the US DOE under contract No. DE-AC02-06CH11357. The work of JJD, GSM and PGK was supported by the US DOE, Office of Science, Office of Basic Energy Sciences, Materials Sciences and Engineering Division under contract No. DE-SC0012704 (Materials Project program KC23MP) at Brookhaven National Laboratory.

#### References

- Baerlocher, C. (1982). *The X-ray Rietveld System (XRS-82), a Set of Computer Programs for the Rietveld Refinement of X-ray Powder Data*. Laboratory of Crystallography, ETH Zürich, Switzerland.
- Bergmann, J., Friedel, P. & Kleeberg, R. (1998). *IUCr Commission on Powder Diffraction Newsletter*, No. 20, pp. 5–8.
- Bertaut, E. F. (1950). *Acta Cryst.* **3**, 14–18.
- Black, D. R., Windover, D., Henins, A., Filliben, J. & Cline, J. P. (2011). *Powder Diffr.* **26**, 155–158.
- Caglioti, G., Paoletti, A. & Ricci, F. P. (1958). *Nucl. Instrum.* **3**, 223–228.
- Cheary, R. W. & Coelho, A. (1992). *J. Appl. Cryst.* **25**, 109–121.
- Cline, J. P., Mendenhall, M. H., Black, D., Windover, D. & Henins, A. (2019). *International Tables for Crystallography*, Vol. H, *Powder Diffraction*, 1st online ed., edited by C. J. Gilmore, J. A. Kaduk & H. Schenk, pp. 224–251. Chester: International Union of Crystallography.
- Coelho, A. (2007). *TOPAS: General Profile and Structure Analysis Software for Powder Diffraction Data*. Coelho Software, Brisbane, Australia.
- Coelho, A. A. (2018). *J. Appl. Cryst.* **51**, 210–218.
- David, W. I. F. (1986). *J. Appl. Cryst.* **19**, 63–64.
- Eddy, M. M., Cheetham, A. K. & David, W. I. F. (1986). *Zeolites*, **6**, 449–454.
- Finger, L. W., Cox, D. E. & Jephcoat, A. P. (1994). *J. Appl. Cryst.* **27**, 892–900.
- Finger, L. W. & Prince, E. (1975). Report 854. National Bureau of Standards, Gaithersburg, Maryland, USA.
- Hastings, J. B., Thomlinson, W. & Cox, D. E. (1984). *J. Appl. Cryst.* **17**, 85–95.
- Hewat, A. (1973). Harwell Report RRL 73, p. 897. UKAERE, Harwell, Didcot, UK.
- Izumi, F. & Ikeda, T. (2000). *Mater. Sci. Forum*, **321–324**, 198–205.
- Kaduk, J. A. & Reid, J. (2011). *Powder Diffr.* **26**, 88–93.
- Klug, H. P. & Alexander, L. E. (1974). *X-ray Diffraction Procedures: For Polycrystalline and Amorphous Materials*, 2nd ed. New York: Wiley.
- Kochendörfer, A. (1943). *Z. Kristallogr.* **105**, 393–480.
- Kril, C. E. & Birringer, R. (1998). *Philos. Mag. A*, **77**, 621–640.
- Laar, B. van & Schenk, H. (2018). *Acta Cryst.* **A74**, 88–92.
- Laar, B. van & Yelon, W. B. (1984). *J. Appl. Cryst.* **17**, 47–54.

- Langford, J. I. (1978). *J. Appl. Cryst.* **11**, 10–14.
- Larson, A. C. & Von Dreele, R. B. (2004). Report LAUR 86-748. Los Alamos National Laboratory, New Mexico, USA.
- Mattei, G. S., Dagdelen, J. M., Bianchini, M., Ganose, A. M., Jain, A., Suard, E., Fauth, F., Masquelier, C., Croguennec, L., Ceder, G., Persson, K. A. & Khalifah, P. G. (2020). *Chem. Mater.* **32**, 8981–8992.
- Mendenhall, M. H., Mullen, K. & Cline, J. P. (2015). *J. Res. Natl Inst. Stand.* **120**, 223–251.
- Patterson, A. L. (1939). *Phys. Rev.* **56**, 978–982.
- Petříček, V., Dušek, M. & Palatinus, L. (2006). *JANA2006*. Institute of Physics, Czech Academy of Sciences, Prague, Czech Republic.
- Prince, E. (2004). *Mathematical Techniques in Crystallography and Materials Science*, 3rd ed. New York: Springer-Verlag.
- Rietveld, H. M. (1967). *Acta Cryst.* **22**, 151–152.
- Rietveld, H. M. (1969). *J. Appl. Cryst.* **2**, 65–71.
- Rodríguez-Carvajal, J. (1993). *Physica B*, **192**, 55–69.
- Scardi, P. & Leoni, M. (2001). *Acta Cryst.* **A57**, 604–613.
- Scherrer, P. (1918). *Nachr. Ges. Wiss. Göttingen*, pp. 98–100.
- Szymanski, N. J., Bartel, C. J., Zeng, Y., Tu, Q. & Ceder, G. (2021). *Chem. Mater.* **33**, 4204–4215.
- Tian, P., Zhou, W., Liu, J., Shang, Y., Farrow, C. L., Juhás, P. & Billinge, S. J. L. (2013). *J. Appl. Cryst.* **46**, 255–258.
- Toby, B. H. & Von Dreele, R. B. (2013). *J. Appl. Cryst.* **46**, 544–549.
- Wiles, D. B. & Young, R. A. (1981). *J. Appl. Cryst.* **14**, 149–151.
- Wilson, A. J. C. (1963). *Mathematical Theory of X-ray Powder Diffractometry*, pp. 1–53. New York: Gordon & Breach.